Journal of the Meteorological Society of Japan

EARLY ONLINE RELEASE

The DOI for this manuscript is
DOI:10.2151/jmsj. 2018-004
J-STAGE Advance published date: November 24, 2017

Thermal Land Surface Emissivity for Retrieving Land Surface Temperature from Himawari-8

Yuhei YAMAMOTO[1]

Disaster Prevention Research Institute, Kyoto University, Kyoto, Japan

and

Hirohiko ISHIKAWA

Disaster Prevention Research Institute, Kyoto University, Kyoto, Japan

May 1, 2017

---

1) Corresponding author: Yuhei Yamamoto, Research Section of Severe Storm and Atmospheric Environment, Division of Atmospheric and Hydrospheric Disasters, Disaster Prevention Research Institute, Kyoto University, Uji, Kyoto 611-0011 JAPAN.
Email: yamamoto_y@storm.dpri.kyoto-u.ac.jp
Tel: +81-774-38-4163
Fax: +81-774-38-4158

Abstract

The land surface emissivity (LSE) in the thermal infrared (TIR) is an essential parameter in the retrieving the land surface temperature (LST) from space. This paper describes the LSE maps in TIR three bands (centered at 10.4, 11.2 and 12.4 μm) used for retrieving the LST from Himawari-8. Himawari-8, a next-generation geostationary satellite has high spatial and temporal resolutions compared to previous geostationary satellites. Due to these improvements, it is expected that the Himawari-8 LST product contribute to observe small-scale environments in high-frequency. In this study, the LSE is estimated by a semi-empirical method, which is a combination of the classification based method and the normalized difference vegetation index (NDVI) thresholds method. The land cover classification information is taken from the Global Land Cover by National Mapping Organizations version3 (GLCNMO 2013). Material emissivities of soil, vegetation and others are taken from the MODIS UCSB emissivity library and the ASTER spectral library. This method is basically following to Peres and DaCamara (2005) but advanced considerations are added. They are phenology of vegetation, flooding of paddy field, snow/ice coverage and the internal reflections (cavity effect) in the urban area. The average cavity effect on LSE in urban canopy is approximately 0.01, but it reaches 0.02 in built-up area. The sensitivity analysis shows that the total LSE

errors for three bands are less than 0.02. The LSE estimation is especially stable at the vegetation area, where the error is less than 0.01.

Keywords land surface emissivity (LSE); Himawari-8; Advanced Himawari Imager (AHI); Land surface temperature (LST); Thermal infrared (TIR); semi-empirical method

1. Introduction

The land surface emissivity (LSE) in the thermal infrared (TIR) is important for the estimation of the land surface temperature (LST) and surface energy budgets. The LST and surface energy budgets are useful for the studies of environmental issues, such as desertification and urban heat islands (Sobrino and Raissouni, 2000; Weng, 2009). The LSE varies depending on various factors, such as the vegetation or soil type, surface roughness and water content. The seasonal change of vegetation also affects the LSE. Even a small LSE estimation error affects the final LST retrieval (Li et al., 2013a). Therefore, it is necessary to consider the various factors affecting the LSE as much as possible. The purpose of this study is to develop the LSE maps in TIR bands used for retrieving the LST from Himawari-8. Himawari-8, the successor to MTSAT-2, was launched in October 2014 and started operational observations in July 2015. This geostationary satellite locates above the equator at longitude 140.7° E and is flying at an altitude of 35786 km. The Advanced Himawari Imager (AHI) onboard Himawari-8 contains three visible bands (band 1, 2 and 3 centered at 0.47, 0.51, and 0.64 μm) and thirteen infrared bands (band 4–16 centered at 0.86, 1.61, 2.25, 3.9, 6.2, 6.9, 7.3, 8.6, 9.6, 10.4, 11.2, 12.4, and 13.3 μm). The spatial resolutions of the visible/near-infrared bands (band 1–4) are 0.5–1.0 km and the infrared bands (band 5–16) are 2.0 km. The observation cycle of the AHI is 2.5 minutes in the area of Japan and 10 minutes for the full disk. The spatial and temporal resolution are

both improved compared to the MTSAT-2. Due to these improvements, the Himawari-8 LST product is expected to contribute to observe small-scale features in high-frequency compared to GMS and MTSAT series. The spectral range 10–12.5 μm in the window thermal infrared is suitable for retrieving land surface temperature using single or multi-channel algorithm (Li et al., 2013a). The AHI has three TIR bands, bands 13, 14 and 15 (centered at 10.4, 11.2 and 12.4μm) in the spectral range of 10–12.5 μm. Therefore, we develop the LSE maps for bands 13, 14 and 15.

Various LSE estimation methods have been proposed for various sensors, which are generally divided into three types (Li et al., 2013b); semi-empirical methods (Snyder et al., 1998; Peres and DaCamara, 2005; Trigo et al., 2008; Sobrino et al., 2008), multi-channel temperature emissivity separation methods (Sobrino et al., 2001; Peres and DaCamara, 2004), and physically based methods (Petitcolin, and Zhang, 2000). Each method has its own advantages and limitations. We employ a semi-empirical method, which is a combination of the classification based method and the normalized difference vegetation index (NDVI) thresholds method. This method is basically following to Peres and DaCamara (2005). The classification based method assigns the predetermined LSE value to each pixel based on the use of a land-cover classification information. The NDVI thresholds method estimates the LSE by considering the surface component as being a mixture of bare soil and vegetation. The visible and near-infrared bands of AHI, bands 3, 4

and 5 (centered at 0.64, 0.86 and 1.61 μm), enable the estimation of the fraction of vegetation, so that it becomes possible to apply the method proposed by Peres and DaCamara (2005). Figure 1 shows the flowchart of our LSE estimation method. Peres and DaCamara (2005) has used the NDVI thresholds method considering the internal reflections (cavity effect) due to the vegetation canopy, but we attempt to consider the cavity effect due to the urban canopy additionally. Furthermore, we consider the seasonal variation of vegetation and specific variation in the paddy field using Himawari-8 visible and near-infrared reflectances. Section 2 describes the NDVI thresholds method and the assignment method to each land cover type. Section 3 describes the predetermined LSE values of soil and vegetation used for the actual observation and the sensitivity analysis for the estimated LSE.

2. Description of Method

2.1 NDVI thresholds method

The NDVI thresholds method has been applied to various sensors (Sobrino and Raissouni, 2000; Sobrino et al., 2008; Valor and Caselles, 1996; Peres and DaCamara, 2005). The method uses the vegetation coverage information in order to estimate the LSE. The LSE is estimated by;

$$LSE = \varepsilon_{v\lambda} FVC + \varepsilon_{g\lambda}(1 - FVC) + d\varepsilon_{\lambda} \quad (1)$$

where ε_v and ε_g are vegetation and ground emissivities, respectively. The subscript λ denotes a center wavelength. The method assumes that a surface state of a pixel is composed of a soil and a vegetation. FVC is the fractional vegetation cover and $d\varepsilon$ is a term representing the cavity effect due to the vegetation canopy (i.e. $d\varepsilon = 0$ for flat surfaces). The non-vegetation area (i.e. FVC = 0) is considered as the flat surface. The FVC is simply obtained from the NDVI and two different NDVI threshold values as (Sobrino and Raissouni, 2000; Sobrino et al., 2008);

$$FVC = \left(\frac{NDVI - NDVI_g}{NDVI_v - NDVI_g} \right)^2 \quad (2)$$

where $NDVI_g$ and $NDVI_v$ are the bare ground and vegetation NDVIs, respectively. Values of $NDVI_g$ = 0.2 and $NDVI_v$ = 0.5 by Sobrino et al. (2008) to apply the method in global conditions are used in this study since they have been applied to various sensors, such as Advanced Very High Resolution Radiometer (AVHRR) onboard the National Oceanic Atmospheric Administration, Spinning Enhanced Visible and IR Imager (SEVIRI) onboard the Meteosat Second Generation, Moderate Resolution Imaging Spectrometer (MODIS) onboard the Terra and Aqua, Advanced Along Track Scanning Radiometer (AATSR) onboard the Environmental Satellite and Thematic Mapper (TM) onboard the LANDSAT-5. In order to estimate FVC in more detail, however, we should recalculate the $NDVI_g$ and $NDVI_v$ values corresponding to observation sites. Of course, FVC is set to zero when NDVI is less than $NDVI_g$ and unity when it is greater than $NDVI_v$. The NDVI is defined as;

$$NDVI = \frac{R_{0.8} - R_{0.6}}{R_{0.8} + R_{0.6}} \quad (3)$$

where $R_{0.8}$ is the reflectance observed in the near-infrared band and $R_{0.6}$ is the reflectance observed in the visible (red) band. In the Himawari observation area, previous studies used the polar-orbiting satellite data because GMS and MTSAT series did not have the near-infrared band. The AHI/Himawari-8, however, has near-infrared band as the band 4. Hence, we used the band 3 and band 4 to estimate the NDVI. The NDVI data is the maximum NDVI in past 14-day composites. Since NDVI depends on solar zenith angle, band 3 and band 4 data within one hour before-and-after the time of culmination at each pixel are used. An atmospheric correction is not applied since the NDVI thresholds method does not basically require an accurate atmospheric correction for estimation of FVC and NDVI (Sobrino et al., 2008; Li et al., 2013b).

The cavity effect term $d\varepsilon$ in Eq. (1) is estimated as;

$$d\varepsilon = (1 - \varepsilon_g)\varepsilon_v F'(1 - FVC) + \left[(1 - \varepsilon_v)\varepsilon_g G' + (1 - \varepsilon_v)\varepsilon_v F''\right]P_s \,. \quad (4)$$

using a simplified geometrical model assuming the infinitely long Lambertian boxes (Caselles and Sobrino, 1989). Here, the P_s is the side proportion observed by the sensor, and F', G' and F'' are geometrical factors that the fraction of radiation emitted by a side that reaches the ground, the proportion emitted by the ground that reaches a side and the fraction emitted by a side that reaches the adjacent one, respectively (see Fig. 2). These geometrical factors are also given by (Caselles and Sobrino, 1989) as

$$F' = (1 + H/S) - \sqrt{1 + (H/S)^2} \ , \quad (5)$$

$$G' = \frac{1}{2}\left[(1 + S/H) - \sqrt{1 + (S/H)^2}\right] \text{ and} \quad (6)$$

$$F'' = \sqrt{1 + (S/H)^2} - S/H \ . \quad (7)$$

Here, H is the height of the hypothetical vegetation elements and S is the distance between them (see Fig. 2). H and S are determined according to a vegetation type. This model does not take into account the shadow influence and double-scattering process. Sobrino et al. (1990) proposed the derivation of P_s considering the case of an observation at a low altitude. In this case, the representation of P_s is quite complicated because P_s of each element in an instantaneous field of view differs greatly depending on satellite zenith angle (SZA) of each element. However, in the case of an observation at a high altitude such as the geostationary satellite, SZAs of each element in an instantaneous field of view are almost same. Hence, we consider the fractional amount by a simplified form without considering the difference of each SZA. Firstly, the simple geometry shows the proportion of the top of cavity element P_t observed by a satellite sensor is constant in SZA θ, whereas the ground proportion P_g linearly decreases as θ increase until the ground disappear from view of the sensor Here, the summation of P_t, P_g and P_s is equal to 1. On the contrary, P_s also increases linearly with θ until the grounds disappear from view of the sensor (until $P_g = 0$), but then after, P_s is constant with increasing θ. Himawari-8 is flying

160 at an altitude of 35786 km and the spatial resolutions of the visible and near-infrared bands
161 are 0.5–1.0 km. Thus, the SZAs that the grounds disappear from view of the AHI in one
162 pixel, θ_d, are almost the same. Accordingly, θ_d, P_t and P_s can be expressed as;

$$\theta_d = arctan\left(\frac{S}{H}\right), \tag{8}$$

$$P_t = \frac{F}{F+S}, \tag{9}$$

$$P_s = \begin{cases} \dfrac{(1-P_t)\theta}{\arctan(S/H)}, & \theta < \theta_d \\ 1 - P_t, & \theta \geq \theta_d . \end{cases} \tag{10}$$

163 where F is the width of a box according to a vegetation type. θ is the satellite zenith angle
164 of the AHI.

165 Peres and DaCamara (2005) assumed that the land surfaces in the urban area are flat
166 and are composed the mixture surfaces of construction concrete and paving asphalts.
167 However, the actual surfaces are rough due to the buildings (urban canopy). Therefore, we
168 consider the cavity effects of urban structures as well as the vegetation. The surface
169 emissivity in urban canopy ε_u is estimated as;

$$\varepsilon_u = \varepsilon_t P_t + \varepsilon_s P_s + \varepsilon_g P_g + d\varepsilon_u \ , \tag{11}$$

$$d\varepsilon_u = (1-\varepsilon_g)\varepsilon_s F' P_g + \left[(1-\varepsilon_s)\varepsilon_g G' + (1-\varepsilon_s)\varepsilon_s F''\right] P_s \ . \tag{12}$$

170 where ε_t and ε_s are top and side emissivities, respectively. That is, we consider a mixture
171 of the roof (ε_t), wall (ε_s) and ground (ε_g). In case an urban pixel includes vegetation, ε_u

substitutes for ε_g in the second term on right side of Eq. (1).

The model assumes that vegetation and urban structures are distributed following infinitely long Lambertian boxes. However, the realistic approximation is the distribution of elements as square finite boxes. Caselles et al. (1997) reported the systematic error due to the use of two different geometric models is of the order of 0.1%.

2.2 Assignment to the land cover class

As mentioned above, the NDVI thresholds method basically requires the five predetermined value and two input data. The predetermined value are the vegetation and ground emissivities ($\varepsilon_{v\lambda}$ and $\varepsilon_{g\lambda}$) of each AHI TIR band and the scales of Lambertian boxes (F, H, and S) according to a vegetation type. The input data is the NDVI and SZA. In order to set the predetermined values according to vegetation type, these values are defined at each pixel based on the land cover class in accordance with Peres and DaCamara (2005). The land cover classification information is taken from the Global Land Cover by National Mapping Organizations (Tateishi et al., 2011; Tateishi et al., 2014; Kobayashi et al., 2017) version3 (GLCNMO 2013). The GLCNMO2013 is based on MODIS data observed in 2013. It employs 20 different land cover classes and the horizontal resolution is about 500 m. Unlike the International Geosphere-Biosphere Program (IGBP) class, it has the paddy field (class 12), mangrove (class 14) and two types of bare areas

191 (classes 16 and 17) additionally. The GLCNMO2013 data was resampled to the resolution
192 of AHI/Himawari-8. The terrestrial surface is nearly 20% of all Himawari-8 main observation
193 area (85 E–155 W, 60 S–60 N), and the percentage of each land cover class is shown in
194 Table 1. Since the rice farming is flourishing in this area, the paddy fields (class 12)
195 accounts for 3.95% of all land cover. When a paddy field pixel is judged as non-vegetated
196 by NDVI criteria, there are two possibilities, one is the dry soil in fallow period and the other
197 the flooding water surface in rice transplanting period. Thus, the paddy field (class 12)
198 should be considered separately from cropland (class 11 or 13). In this sense,
199 GLCNMO2013 is suitable for the LSE estimation in Asian area.

200 The NDVI threshold method is applied to the classes 1–14 and 16–18. The classes 15
201 (Wetlands) and 19 (Snow/Ice) are given constant emissivity values regardless to seasonal
202 changes of vegetation. In terms of the vegetation emissivity, we used the TIR volumetric
203 bidirectional reflectance distribution function (BRDF) model (Snyder and Wan, 1998) to
204 calculate the BRDF and integrate it over the hemisphere to obtain the directional
205 hemispherical reflectance (DHR) and emissivity from reflectance of each leaf, bark or grass
206 sample measured by laboratories. The TIR volumetric BRDF model form is:

$$f_{vol} = c_1 k_{vol}^{\rho} + c_2 k_{vol}^{\tau} + c_3 \quad (13)$$

207 the kernels are given by

$$k_{vol}^{\rho} = \frac{(\pi - \xi)cos\xi + sin\xi}{cos\theta_i + cos\theta_r} - \frac{\pi}{2}, \quad (14)$$

$$k_{vol}^{\tau} = \frac{-\xi cos\xi + sin\xi}{cos\theta_i + cos\theta_r}, \quad (15)$$

208 and the coefficients by

$$c_1 = \frac{2\rho}{3\pi^2}[1 - \exp(-bF)], \quad (16)$$

$$c_2 = \frac{2\tau}{3\pi^2}[1 - \exp(-bF)], \quad (17)$$

$$c_3 = \frac{\rho}{3\pi}[1 - \exp(-bF)] + \frac{\rho_0}{\pi}[\exp(-bF)]. \quad (18)$$

209 here θ_i and θ_r are the incident zenith angle and reflected zenith angle; ρ is the leaf, bark
210 or grass reflectance and ρ_0 is the ground reflectance; τ is the leaf transmission; bF is
211 the optical depth; ξ is the scattering angle between incidence and reflection. ξ is given by:

$$\xi = \arccos(cos\theta_i cos\theta_r + sin\theta_i sin\theta_r cos\phi) \quad (19)$$

212 where, ϕ is the relative azimuth angle between the incident and reflected directions. τ is
213 taken to be zero for the TIR region and bF is taken to be infinite (Snyder and Wan, 1998).
214 Therefore, this model requires not a ground reflectance ρ_0 but a leaf, bark or grass
215 reflectance ρ to determine the volumetric BRDFs f_{vol}. The leaf, bark and grass
216 emissivities for each TIR band are weighted by the spectral response function of each TIR
217 band. Table 2 shows the leaf, bark and grass samples assigned to land cover types. These
218 samples were selected from the MODIS UCSB emissivity library

(http://www.icess.ucsb.edu/modis/EMIS/html/em.html; Wan et al., 1994) and the ASTER spectral library (http://speclib.jpl.nasa.gov/; Baldridge et al., 2009) and were based on the available spectra as representing the general features of trees though more kinds of vegetation should be considered. The seasonal change of vegetation is considered as green and senescent states (Snyder et al., 1998). The seasonal states, green or senescent of each pixel are judged by using the maximum NDVI in past 14-day composites and the annual mean NDVI value consist of 12 periods of 30-day composite as the thresholds. If the maximum NDVI in past 14-day composites of a pixel is greater (smaller) than the annual mean NDVI of the same pixel, the seasonal state of the pixel is judged as green (senescent). The combination ratios of classes 5–10, class 13 and classes 15–18 were determined by referring to Peres and DaCamara (2005). The vegetation emissivity ($\varepsilon_{v\lambda}$) used for the predetermined value is considered as the mean value of the vegetation emissivities of the materials for each class.

The paddy field (class 12) has three characteristics periods, such as the flooding and rice transplanting period, the growing period and the fallow period (Xiao et al., 2002). The state for the paddy field is sub-divided as shown in Table 2. The growing period in the green state may means vegetative growth stage or reproductive stage, while the growing or the fallow period in the senescent state may mean ripening stage or weeds in the fallow period. In order to judge the flooding and rice transplanting period, the difference between

238 normalized difference water index (NDWI) and NDVI values (Xiao et al., 2002) consist of
239 14-day composites is used. The NDWI is defined as;

$$NDWI = \frac{R_{0.8} - R_{1.6}}{R_{0.8} + R_{1.6}} \quad (20)$$

240 where $R_{0.8}$ and $R_{1.6}$ are the reflectance of near-infrared observed in band 4 and band 5
241 of AHI, respectively. If a pixel of paddy field has smaller NDVI than NDWI, the pixel is
242 judged as water body and is considered as the wetland (class 15).

243 The ground emissivity is also evaluated based on the MODIS UCSB emissivity library
244 and the ASTER spectral library. Each land class is assumed to be covered by materials
245 listed in Table 3. The gross emissivity of each material, for example 'Inceptisol', is
246 computed by integrating the spectral emissivity in library with the weight of sensor response
247 function over the band width. When sub-materials exist, the value is averaged over the
248 sub-materials. It is worth noting that classes 15 (Wetlands) and 19 (Snow/Ice) are also
249 listed in Table 3 though the NDVI threshold method is not applied. The ground emissivity of
250 each class ($\varepsilon_{g\lambda}$) is computed as the mean over component materials in Table 3. The Table
251 3 is modified from the corresponding table in Peres and DaCamara (2005) considering the
252 difference in soil components Asia and Oceania from Europe and Africa region. The soil
253 and rock materials of each land cover are decided by referring to the global soil regions
254 map (https://www.nrcs.usda.gov/wps/portal/nrcs/detail/soils/use/?cid=nrcs142p2_054013).
255 The soil type under broadleaf evergreen forest (class 1) in the tropical zone, is actually

256 ‘ultisols’ but is assumed as in Table 3. It is because the ‘ultisols’ are not included in ASTER
257 library, but it may not cause much problem since the ground surfaces are usually covered
258 by the crown canopy and the forest floor in these tropical forests. The ground material in the
259 mangrove (class 14) is set as water, though it has a property of broadleaf evergreen forest.
260 For the snow/ice surfaces, the areas other than class 19 sometimes be also covered by
261 snow or ice. Considering this case, the snow/ice surfaces are detected using the
262 normalized difference snow and ice index (NDSII) in addition to the region in class 19. The
263 NDSII is defined as (Xiao et al., 2001);

$$NDSII = \frac{R_{0.6} - R_{1.6}}{R_{0.6} + R_{1.6}} \tag{21}$$

264 The NDSII data is obtained by past 4-day composites. When NDSII of a pixel is greater
265 than 0.4, the mean emissivity of snow and ice is assigned to the pixel. Although the
266 atmospheric correction is required to calculate the NDWI, NDVI and NDSII in more detail, it
267 is not considered and is a future task in this study.

268 Table 4 shows the scales of Lambertian boxes (F, H, and S) of each vegetation type.
269 These values were set based on Sobrino et al. (1990), Valor and Caselles (1996) and
270 Peres and DaCamara (2005). The forest regions are assumed to be short separation and
271 high boxes. Shrub, sparse and unforested regions are assumed to be long separation and
272 low boxes. The length assumed at each face has a reasonable range. We calculate all $d\varepsilon$
273 by combinations of three lengths and then consider the mean $d\varepsilon$ as the representative

274 value of each class.

275 Since we are to use the retrieved LST to the research in urban environment study, a
276 special attention is payed for urban canopy effect. The geometrical model for surface
277 emissivity in urban area also requires the surface emissivities of the top, side and ground of
278 each AHI TIR band and the scales of Lambertian boxes (F, H, and S) according to urban
279 canopy. Table 5 shows the manmade materials and the scales applied to each face of
280 urban structure. The scales of urban structure were based on Moriwaki et al. (2002),
281 Strømann-Andersen and Sattrup (2011) and Ito et al. (2015). The roofing (top) materials
282 are considered the rubbers and shingles except for the metals. The wall (side) materials are
283 considered the construction concretes except for bricks, window glasses, paints and woods.
284 The urban structures have various characteristics by a degree of development, such as
285 commercial, industrial and residential area. Although it is possible to set values
286 corresponding to each urban structure by using more detailed land use data (Yang et al.,
287 2015a, b), we made a rough estimate by assuming an average structure. The mean $d\varepsilon_u$ of
288 all combinations of three lengths are calculated as the representative cavity effect due to
289 the urban canopy. Note that the internal reflection due to the trees cannot occur over the
290 roof faces since assumed building height is higher than the assumed tree height in Table 3.
291 Therefore, when we calculate the cavity effect in urban area due to the trees using Eq. (4),
292 the ground emissivities are considered as consisting construction concretes, road asphalts

and tar, not ε_u (Eq. 11).

3. Results and Discussions

3.1. Vegetation and ground emissivity

Table 6 and 7 show the emissivities of vegetation and ground for each land cover class as derived by the procedure described in the previous section. For the vegetation, both green and senescent states are listed. The deviation (Dev.) is computed by considering the experimental error of each component material consisting a class. The experimental errors of emissivity in the laboratory and the field measurements are assumed as ± 0.005 (Caselles et al., 1997). The 'Dev.' is calculated as;

$$\text{Dev.} = \sqrt{\frac{1}{3n-1}\left\{\sum_{i=1}^{n}(\varepsilon_i - \bar{\varepsilon})^2 + \sum_{i=1}^{n}(\varepsilon_i + 0.005 - \bar{\varepsilon})^2 + \sum_{i=1}^{n}(\varepsilon_i - 0.005 - \bar{\varepsilon})^2\right\}} \quad (22)$$

where n is a number of component materials of each class and $\bar{\varepsilon}$ is mean emissivity of each class. The vegetation has basically higher emissivity and lower deviation than soils or rocks. The senescent vegetation has lower emissivity and higher deviation than the green vegetation. The class 16 (bare area, consolidated) has the lowest emissivity and the highest deviation in the ground emissivity. Table 8 shows the emissivity and deviation at each face of urban structure corresponding to Table 5. The deviations are also calculated considering ± 0.005 experimental error of component materials. The deviation is high

310 especially at the top. This is because the roofing materials have a large variety in emissivity.
311 The values for band 13, 14, 15 range, respectively, from 0.8598 to 0.9661, 0.9177 to
312 0.9725 and 0.9288 to 0.9808. If the metal roofing materials and window glasses are
313 considered, there is a possibility of higher deviation because these emissivities are quite
314 low less than 0.8.
315
316 *3.2. Magnitude of the cavity effect*
317 The cavity effect of vegetation, $d\varepsilon$, is shown in Fig. 3 as functions of SZA and FVC for
318 the green state. The left-hand column of Fig. 3 shows the SZA dependences of $d\varepsilon$ for
319 three TIR bands. They were calculated assuming the FVC = 0.5. The right-hand column
320 shows the FVC dependences for three TIR bands. They were calculated assuming the SZA
321 = 20 °. $d\varepsilon$ values are greatly varied with vegetation type, and $d\varepsilon$ of classes 1, 2, 3, 4 and
322 5 are especially high. Conversely, $d\varepsilon$ of the regions assumed low-height trees and
323 long-separation between them, such as classes 10, 16, 17, 18 are less than 0.01. Thus, we
324 may not consider the cavity effects in those regions. The $d\varepsilon$ slightly increases with
325 increasing SZA, while it obviously decreases with increasing FVC. In reality, the FVC (the
326 side proportion) is not constant but increases with increasing SZA. Therefore, as mentioned
327 by Valor and Caselles (1996), it is considered that $d\varepsilon$ decreases with increasing SZA.
328 The cavity effect due to the urban structure, $d\varepsilon_u$, for SZA ranging from 0° to 60° is shown

329 in Table 9. The $d\varepsilon_u$ of band 13 and 14 are greater than 0.01 for all the SZAs and $d\varepsilon_u$ of
330 band 15 is approximately 0.01. Atitar and Sobrino, (2009) reported that the emissivity error
331 greater than 0.01 causes the LST retrieval error of approximately 1 K. Hence, it is
332 necessary to consider the cavity effect in the urban areas same as the vegetation. Yang et
333 al. (2015a) estimated the LSE in TIR band of the Landsat 8 in urban area using the building
334 GIS data. They reported the differences reach 0.02 between the material emissivity and
335 effective emissivity considered the cavity effect especially over built-up areas. Table 10
336 shows the urban surface emissivity ε_u and $d\varepsilon_u$ of two geometrical shapes; one has a
337 large $d\varepsilon_u$ (type A: F = 10 m, H = 15 m, S = 20 m) and the other has a small $d\varepsilon_u$ (type B: F
338 = 20 m, H = 7 m, S = 10 m) for three TIR bands in the SZA ranging from 0° to 60° at
339 intervals of 20°. The ε_u and $d\varepsilon_u$ differences between type A and B are shown at the
340 bottom of the Table 10. Both types of A and B are assumed for estimation of $d\varepsilon_u$ in this
341 study as shown in Table 5. $d\varepsilon_u$ of type A for band 13 certainly reaches 0.02. The ε_u and
342 $d\varepsilon_u$ differences between type A and B for band 13, 14 are greater than 0.01. Therefore, if
343 we observe the urban areas in more detail, it should require the land use data having a
344 higher spatial resolution, such as the building GIS data. The similar sophisticated method
345 may be possible for other vegetation and/or bare soil areas, if the detailed *in situ* database
346 is available. Then, it will be possible to acquire the more detail ε_v, ε_u (ε_g), F, H, S
347 information.

348

349 *3.3. Seasonal and dynamic changes of LSE*

350 Figure 4 shows the time changes of LSEs for three AHI TIR bands, NDVI and NDSII over
351 a cropland in Japan (42.74°N, 143.14°E) from August 2015 to December 2015. The NVDI
352 decreases gradually through the observed term. On the other hand, the LSEs suddenly
353 decrease in late October when NDVI becomes smaller than a threshold for the judgment of
354 seasonal state of the pixel. After the decrease, the LSEs are constant or a little increasing.
355 In this period, the cavity effect of vegetation increases with decreasing FVC in November.
356 In December, the sudden changes of the NDSII and LSEs due to snow/ice coverage are
357 observed.

358 When a land surface is covered by snow/ice, the observed value of NDVII becomes low.
359 Thus, a LSE estimation error due to the misjudgment of snow/ice coverage is almost same
360 as the difference between ground emissivity of each class and snow/ice emissivity of class
361 19 (see Table 7).

362 Figure 5 shows the time changes of LSEs for three AHI TIR bands, NDVI and NDWI over
363 a paddy field in Japan (37.58°N, 138.85°E) from April 2016 to June 2016. The NDVI is
364 generally larger than the NDWI. However, the NDWI becomes larger than the NDVI from
365 May to early June. This is due to the flooding and rice transplanting. The LSEs change
366 according to this inversion of the relation between NDVI and NDWI. If the NDWI is not

367 considered, the LSE for the flooding and rice transplanting period is assigned as near the
368 value of ground emissivity. Thus, the LSE estimation error due to the misjudgment of
369 flooding is near the difference between the ground emissivity of class 12 and the emissivity
370 of class 15 (see Table 7). The misjudgments of seasonal and dynamic states, such as
371 senescent vegetation, snow/ice coverage and flooding in the paddy field may cause large
372 LSE error. Although these are the inherent disadvantages of the classification based
373 method and the NDVI thresholds method, our considerations using NDSII and NDWI
374 reduce the errors.
375
376 *3.4. Sensitivity analysis*
377 The *in-situ* evaluation of LSE is practically impossible, so that we assess the possible
378 total LSE error for each class instead. We perform a sensitivity analysis as regard to input
379 data. Based on Eq. (1) – (10), the total LSE error is defined as (Caselles et al., 1997)

$$\delta\varepsilon_\lambda = \left|\frac{\partial\varepsilon_\lambda}{\partial\varepsilon_{\lambda v}}\right|\delta\varepsilon_{\lambda v} + \left|\frac{\partial\varepsilon_\lambda}{\partial\varepsilon_{\lambda g}}\right|\delta\varepsilon_{\lambda g} + \left|\frac{\partial\varepsilon_\lambda}{\partial P_v}\right|\delta FVC + \left|\frac{\partial\varepsilon_\lambda}{\partial F}\right|\delta F + \left|\frac{\partial\varepsilon_\lambda}{\partial H}\right|\delta H + \left|\frac{\partial\varepsilon_\lambda}{\partial S}\right|\delta S \quad (23)$$

380 The emissivity errors of each class ($\delta\varepsilon_{\lambda v}$ and $\delta\varepsilon_{\lambda g}$) are computed by considering ± 0.005
381 experimental errors for all materials and bands (i.e., these errors are equal to Dev. of each
382 class as shown in Table 6 and 7). F, H and S errors are assumed as 10% of their value (i.e.,
383 δF, δS and δH are the deviations corresponding to the errors of $\pm 0.1F$, $\pm 0.1S$ and
384 $\pm 0.1H$). For example, when we calculate δF for F = 1.0 m of the class 1, δF is calculated

as $\sqrt{\frac{1}{2}\{(1.1-1.0)^2+(0.9-1.0)^2\}}$. These emissivity and shape errors are based on Caselles et al. (1997). For the proportions of F, H and S, Caselles et al. (1997) considered a mixed pixel of FVC = 0.5 and an SZA of P_s = 0.2 and P_t = 0.3. Instead, we consider a situation; FVC = 0.5 and SZA = 20°. On this basis, the FVC estimation error is assumed to vary between 5 % and 25 %, which is an appropriate estimation error range based on vegetation indices (Caselles et al., 1997; Peres and DaCamara, 2005). Urban canopy is additionally considered in this study. Therefore, instead of $\delta\varepsilon_{\lambda g}$, for urban area, $\varepsilon_{\lambda gu}$, is calculated by

$$\delta\varepsilon_{\lambda gu} = \left|\frac{\partial\varepsilon_\lambda}{\partial\varepsilon_{\lambda t}}\right|\delta\varepsilon_{\lambda t} + \left|\frac{\partial\varepsilon_\lambda}{\partial\varepsilon_{\lambda s}}\right|\delta\varepsilon_{\lambda s} + \left|\frac{\partial\varepsilon_\lambda}{\partial\varepsilon_{\lambda g}}\right|\delta\varepsilon_{\lambda g} + \left|\frac{\partial\varepsilon_\lambda}{\partial F}\right|\delta F + \left|\frac{\partial\varepsilon_\lambda}{\partial H}\right|\delta H + \left|\frac{\partial\varepsilon_\lambda}{\partial S}\right|\delta S \quad (24)$$

The top, side and ground emissivity errors, $\delta\varepsilon_{\lambda t}$, $\delta\varepsilon_{\lambda s}$ and $\delta\varepsilon_{\lambda g}$, are computed by considering ± 0.005 experimental errors for all materials and bands (i.e., these errors are equal to Dev. of each class as shown in Table 8). F, H and S errors for urban canopy are also assumed as 10% of their value.

Figure 6 shows the total LSE error of each GLCNMO class and TIR band for two seasonal states. The left-hand column of Fig. 6 is for the green state and the right-hand column is for the senescent state. The total LSE error for senescent state is excluded the evergreen-vegetation classes (classes 1, 3 and 14), class 15 (wetland) and class 19 (snow/ice). Since the NDVI thresholds method is not applied to the classes 15 and 19, they are not affected by the FVC estimation error. The LSE error for band 13 is the highest of the

three TIR bands. While the errors of most classes for band 14 and 15 are less than 0.01, the errors of classes 16 and 18 for band 13 are greater than 0.01 and especially the error of class 18 reaches approximately 0.015. It is thought that the error of class 16 is caused by the large deviation of ground emissivity (see Table 7) and the error of class 18 is caused by not only the large deviation of ground and top emissivity (see Table 8) but also the large instability of $d\varepsilon_u$ due to urban surface structure (see Table 10). On the other hand, the areas classified as the forest (classes 1, 2, 3, 4, 5 and 14) have the quite low LSE errors, even the LSE errors for band 13 are less than 0.005. Furthermore, the influences of the FVC estimation error for these classes are very small.

The above results except for urban (class 18) have the estimation accuracy comparable to previous studies with the semi-empirical method (Snyder et al., 1998; Peres and DaCamara, 2005). For the urban area, it is obvious that the large LSE error occurred in the spatial resolution of global map (approximately 0.01°) by making a rough estimate of urban surface structure.

3.5. Possible misclassification in GLCNMO2013

The LSE error due to misclassification of land cover map should also be considered. Kobayashi et al. (2017) reported the misclassification ratio of GLCNMO2013, in that classification accuracies in some forest types (classes 2-11 and 13) are low. The “user’s

422 accuracies" of these classes range from 47% to 79% and "the producer's accuracies" range
423 from 48% to 74%. Evergreen forest (class 1) and mangrove (class 14) have more than 84%
424 of user's accuracies and more than 90% of producer's accuracies. Paddy field (class 12)
425 has 84% of user's accuracy and 77% of producer's accuracy. It is generally difficult to
426 distinguish among different forest types, so that the similar tendency of misclassification is
427 found in other global land cover maps, such as the International Geosphere-Biosphere
428 Program Data and Information System (IGBP-DIS) and the MODIS MOD12Q1 land-cover
429 product (Peres et al., 2005). For other classes, wetland (class 15) has 87% of user's
430 accuracy and 65% of producer's accuracy. Bare area, consolidated (class 16) has 78% of
431 user's accuracy and 76% of producer's accuracy. Bare area, unconsolidated (class 17) has
432 89% of user's and producer's accuracies. Urban (class 18) has 100% of user's accuracy
433 and 98% of producer's accuracy. Snow/ice (class 19) has 98% of user's and producer's
434 accuracies.

435 The misclassification is most likely to occur within different vegetation classes. Both
436 vegetation and ground emissivity differences between vegetation classes for the green
437 state are less than 0.01 for three bands (see Table 6 and 7). For the senescent state,
438 however, the vegetation emissivity difference may reach to about 0.015 (e.g., the difference
439 between classes 7 and 8 in band 14). Another source of the misclassification resides in
440 bare areas (classes 16 and 17), which may cause larger LSE error (about 0.02–0.05). As

described in the section 2.2, different emissivity assignment methods are applied to the paddy field, urban, wetland and snow/ice. The misclassification in these classes leads to the misapplication between the methods, which may cause large LSE error. Fortunately, paddy field, urban, wetland and snow/ice have high classification accuracies. Therefore, it is thought that the misapplication of emissivity assignment is expected to small.

3.6. Influence on LST estimation

Yamamoto et al. (2017) evaluated the sensitivities of their newly developed LST algorithm, nonlinear three-band algorithm, to the uncertainties of LSEs for three bands (± 0.02) and compared with other existing algorithms, nonlinear split-window algorithm by Sobrino and Romaguera (2004) and three-band algorithm by Sun and Pinker (2003). The nonlinear three-band algorithm has a LST calculation formula which is improved by adding quadratic terms of the difference between 2 brightness temperatures into the three-band algorithm by Sun and Pinker (2003). The algorithm makes the maximum use of AHI window TIR bands, bands 13, 14 and 15. It is reported that the LST estimation error caused by the ± 0.02 LSE uncertainties for the nonlinear split-window, three-band and nonlinear three-band algorithms are 2.90 K, 3.00 K and 1.84 K (at nadir), respectively. The sensitivity analysis for LSE estimation (Fig. 6) ensures smaller LST estimation error than their derived LST errors. The misjudgments of seasonal and dynamic states may cause ± 0.02 LSE error

460 in maximum, which in turn yield the LST error evaluated by Yamamoto et al. (2017).
461 Therefore, the LSE error influence on the final LST retrieval accuracy is concluded within
462 the allowable range. Only the misclassification in bare areas (classes 16 and 17), however,
463 may cause larger LST error since the ground emissivity difference between them is large.
464
465 **4. Conclusions**
466 The LSE maps for AHI three TIR bands were developed by using a semi-empirical
467 method based on Peres and DaCamara (2005). These are to be used in the LST retrieval
468 from Hiamwari-8. Peres and DaCamara (2005) assigned the emissivity value of the mixture
469 of vegetation and soil to each pixel based on the IGBP land cover class. The fractional
470 vegetation cover of each pixel is estimated from the NDVI observation. Because the AHI
471 also has visible and near-infrared bands which is needed to calculate the NDVI, it becomes
472 possible to apply their method. In this study, the land cover classification information is
473 taken from the GLCNMO2013 and material emissivities of soil, vegetation and others are
474 taken from the MODIS UCSB emissivity library and the ASTER spectral library.
475 We newly added three considerations over Peres and DaCamara (2005). In order to
476 consider phenology, two seasonal states, green and senescent, are considered by using
477 the NDVI value on the basis of the annual mean NDVI consist of 12 periods of 30-day
478 composite. Accordingly, slightly lower emissivity is assigned to the senescent state and

479 higher emissivity value is assigned to the green state. Secondly, the flooding and rice
480 transplanting period in the paddy fields and snow/ice coverage are detected using the
481 NDWI, NDVI and NDSII. When a pixel is covered by snow/ice, the emissivity value of
482 snow/ice is assigned independent to the pixel class. For paddy fields, when a pixel is
483 judged as the flooding and rice transplanting period, the high emissivity value that has both
484 grass and water properties is assigned. Thirdly, the cavity effect due to the urban canopy is
485 considered by extending the geometrical model for vegetation canopy proposed by
486 Caselles and Sobrino, (1989). Several typical urban structures and the gross emissivity of
487 each face of urban structure are assumed. Peres and DaCamara (2005) assumed that the
488 land surfaces in the urban area are flat, and reported that the estimation error was low.
489 However, our result shows that the average value of the cavity effect on LSE is as large as
490 0.01 and it varies greatly depending on the urban structure. It reaches to 0.02 especially
491 over built-up area. The total LSE error is also estimated. It was especially high in urban
492 area. Thus, it is obvious that the cavity effect of urban structure cannot be ignored even in
493 global (approximately 1 km) scale.

494 The sensitivity analysis shows that the total LSE errors for three bands are less than 0.02.
495 The error is especially stable at the vegetation area, where it is less than 0.01. However, we
496 have to pay attention to the misclassification in bare areas and the misjudgments of
497 seasonal and dynamic states, which may cause large LSE error. Because this accuracy of

498 the LSE is comparable to that of previous studies (Snyder et al., 1998; Peres and
499 DaCamara, 2005), the LSE maps are sufficiently applicable to the multi-channel LST
500 algorithm, such as a split-window algorithm and a three-band algorithm. Our LSE product
501 may also provide initial-guess estimates for the two-temperature method (TTM) that
502 retrieve the LST and LSE simultaneously (Peres and DaCamara, 2004).
503
504 **Acknowledgments**
505 Himawari 8/9 gridded data and the Global Map-Global Land Cover (GLCNMO) version 3
506 are distributed by Center for Environmental Remote Sensing (CEReS), Chiba University,
507 Japan.
508
509 **References**
510
511 Atitar, M., and J. A. Sobrino, 2009: A split-window algorithm for estimating LST from
512 meteosat 9 data: Test and comparison with in situ data and MODIS LSTs. *IEEE*
513 *Geosci. Remote Sens. Lett.*, **6**, 122–126, doi:10.1109/LGRS.2008.2006410.
514 Baldridge, A. M., S. J. Hook, C. I. Grove, and G. Rivera, 2009: The ASTER spectral library
515 version 2.0. *Remote Sens. Environ.*, **113**, 711–715, doi:10.1016/j.rse.2008.11.007.
516 http://dx.doi.org/10.1016/j.rse.2008.11.007.

517 Caselles, V., and J. A. Sobrino, 1989: Determination of frosts in orange groves from
518 NOAA-9 AVHRR data. *Remote Sens. Environ.*, **29**, 135–146, doi:10.1016/0034-4257
519 (89)90022-9.
520 Caselles, V., E. Valor, C. Coll, and E. Rubio, 1997: Thermal band selection for the PRISM
521 instrument: 1. Analysis of emissivity-temperature separation algorithms. *J. Geophys.*
522 *Res.*, **102**, 11145–11164, doi:10.1029/97JD00344.
523 Ito, R., T. Satomura, and T. Takemi, 2015: Idealized experiments on the development of
524 urban warming under various geographical conditions using a meso-scale
525 meteorological model. *ICUC9 - 9th International Conference on Urban Climate jointly*
526 *with 12th Symposium on the Urban Environment*.
527 Kobayashi, T., Tateishi, R., Alsaaideh, B., Sharma, R.C., Wakaizumi, T., Miyamoto, D., Bai,
528 X., Long, B.D., Gegentana, G., Maitiniyazi, A., Cahyana, D., Haireti, A., Morifuji, Y.,
529 Abake, G., Pratama, R., Zhang, N., Alifu, Z., Shirahata, T., Mi, L., Iizuka, K.,
530 Yusupujiang, A., Rinawan, F.R., Bhattarai, R., Phong, D.X., 2017: Production of Global
531 Land Cover Data – GLCNMO2013. *J. Geogr. Geol.*, **9**, 1, doi:10.5539/jgg.v9n3p1.
532 http://www.ccsenet.org/journal/index.php/jgg/article/view/67828.
533 Li, Z., B. Tang, H. Wu, H. Ren, G. Yan, Z. Wan, I. F. Trigo, and J. a Sobrino, 2013a:
534 Satellite-derived land surface temperature: Current status and perspectives. *Remote*
535 *Sens. Environ.*, **131**, 14–37, doi:10.1016/j.rse.2012.12.008. http://www.scopus.com/in

536 ward/record.url?eid=2-s2.0-84872361145&partnerID=40&md5=a4f2a29bdcfc5f0fc068
537 c983a6eba3f3.
538 Li, Z.-L., H. Wu, N. Wang, S. Qiu, J. A. Sobrino, Z. Wan, B.-H. Tang, and G. Yan, 2013b:
539 Land surface emissivity retrieval from satellite data. *Int. J. Remote Sens.*, **34**, 3084–
540 3127, doi:10.1080/01431161.2012.716540. http://www.scopus.com/inward/record. ur
541 l?eid=2-s2.0-84873680527&partnerID=tZOtx3y1.
542 Moriwaki, R., M. Kanda, T. Watanabe, and K. Matsunaga, 2002: Estimation of land-surface
543 parameters in urban boundary layer (In Japanese). *Proc. Hydraul. Eng.*, **46**, 91–96,
544 doi:10.2208/prohe.46.91.
545 Peres, L. F., and C. C. DaCamara, 2004: Land surface temperature and emissivity
546 estimation based on the two-temperature method: Sensitivity analysis using simulated
547 MSG/SEVIRI data. *Remote Sens. Environ.*, **91**, 377–389, doi:10.1016/j.rse.2004.03.0
548 11.
549 Peres, L. F., and C. C. DaCamara, 2005: Emissivity maps to retrieve land-surface
550 temperature from MSG/SEVIRI. *IEEE Trans. Geosci. Remote Sens.*, **43**, 1834–1844,
551 doi:10.1109/TGRS.2005.851172.
552 Petitcolin, F., and E. Vermote, 2002: Land surface reflectance, emissivity and temperature
553 from MODIS middle and thermal infrared data. *Remote Sens. Environ.*, **83**, 112–134,
554 doi:10.1016/S0034-4257(02)00094-9.

555 Snyder, W. C., and Z. Wan, 1998: BRDF models to predict spectral reflectance and
556 emissivity in the thermal infrared. *IEEE Trans. Geosci. Remote Sens.*, **36**, 214–225,
557 doi:10.1109/36.655331.
558 Snyder, W. C., Z. Wan, Y. Zhang, and Y.-Z. Feng, 1998: Classification-based emissivity for
559 land surface temperature measurement from space. *Int. J. Remote Sens.*, **19**, 2753–
560 2774, doi:10.1080/014311698214497.
561 Sobrino, J. A., V. Caselles, and F. Becker, 1990: Significance of the remotely sensed
562 thermal infrared measurements obtained over a citrus orchard. *ISPRS J. Photogramm.*
563 *Remote Sens.*, **44**, 343–354, doi:10.1016/0924-2716(90)90077-O.
564 Sobrino, J. A., J. C. Jiménez-Muñoz, G. Sòria, M. Romaguera, L. Guanter, J. Moreno, A.
565 Plaza, and P. Martínez, 2008: Land surface emissivity retrieval from different VNIR and
566 TIR sensors. *IEEE Trans. Geosci. Remote Sens.*, **46**, 316–327, doi:10.1109/TGRS. 20
567 07.904834.
568 Sobrino, J. A., and N. Raissouni, 2000: Toward remote sensing methods for land cover
569 dynamic monitoring: Application to Morocco. *Int. J. Remote Sens.*, **21**, 353–366,
570 doi:10.1080/014311600210876.
571 Sobrino, J. A., N. Raissouni, and Z.-L. Li, 2001: A Comparative Study of Land Surface
572 Emissivity Retrieval from NOAA Data. *Remote Sens. Environ.*, **75**, 256–266,
573 doi:10.1016/S0034-4257(00)00171-1.

574 Sobrino, J. A., and M. Romaguera, 2004: Land surface temperature retrieval from
575 MSG1-SEVIRI data. *Remote Sens. Environ.*, **92**, 247–254,
576 doi:10.1016/j.rse.2004.06.009.
577 Strømann-Andersen, J., and P. A. Sattrup, 2011: The urban canyon and building energy
578 use: Urban density versus daylight and passive solar gains. *Energy Build.*, **43**, 2011–
579 2020, doi:10.1016/j.enbuild.2011.04.007.
580 Sun, D., and R. T. Pinker, 2003: Estimation of land surface temperature from a
581 Geostationary Operational Environmental Satellite (GOES-8). *J. Geophys. Res.*, **108**,
582 4326, doi:10.1029/2002JD002422. http://doi.wiley.com/10.1029/2002JD002422.
583 Tateishi, R., and Coauthors, 2011: Production of global land cover data – GLCNMO. *Int. J.*
584 *Digit. Earth*, **4**, 22–49, doi:10.1080/17538941003777521.
585 Tateishi, R., N. T. Hoan, T. Kobayashi, B. Alsaaideh, G. Tana, and D. X. Phong, 2014:
586 Production of Global Land Cover Data – GLCNMO2008. *J. Geogr. Geol.*, **6**, 99,
587 doi:10.5539/jgg.v6n3p99.
588 http://www.ccsenet.org/journal/index.php/jgg/article/view/37581.
589 Trigo, I. F., L. F. Peres, C. C. DaCamara, and S. C. Freitas, 2008: Thermal land surface
590 emissivity retrieved from SEVIRI/Meteosat. *IEEE Trans. Geosci. Remote Sens.*, **46**,
591 307–315, doi:10.1109/TGRS.2007.905197.
592 Valor, E., and V. Caselles, 1996: Mapping land surface emissivity from NDVI: Application to

593 European, African, and South American areas. *Remote Sens. Environ.*, **57**, 167–184,
594 doi:10.1016/0034-4257(96)00039-9.
595 Weng, Q., 2009: Thermal infrared remote sensing for urban climate and environmental
596 studies: Methods, applications, and trends. *ISPRS J. Photogramm. Remote Sens.*, **64**,
597 335–344, doi:10.1016/j.isprsjprs.2009.03.007. http://dx.doi.org/10.1016/j.isprsjprs.200
598 9.03.007.
599 Xiao, X., Z. Shen, and X. Qin, 2001: Assessing the potential of VEGETATION sensor data
600 for mapping snow and ice cover: A Normalized Difference Snow and Ice Index. *Int. J.*
601 *Remote Sens.*, **22**, 2479–2487, doi:10.1080/01431160119766.
602 Xiao, X., S. Boles, S. Frolking, W. Salas, B. Moore, C. Li, L. He, and R. Zhao, 2002:
603 Observation of flooding and rice transplanting of paddy rice fields at the site to
604 landscape scales in China using VEGETATION sensor data. *Int. J. Remote Sens.*, **23**,
605 3009–3022, doi:10.1080/01431160110107734.
606 Yamamoto, Y. and H. Ishikawa, Y. Oku, 2017: An algorithm for land surface temperature
607 retrieval using three thermal infrared bands of Himawari-8. J. Meteor. Soc. Japan. “in
608 press”.
609 Yang, J., M. S. Wong, M. Menenti, and J. Nichol, 2015a: Modeling the effective emissivity
610 of the urban canopy using sky view factor. *ISPRS J. Photogramm. Remote Sens.*, **105**,
611 211–219, doi:10.1016/j.isprsjprs.2015.04.006.

612 Yang, J., M. S. Wong, M. Menenti, and J. Nichol, 2015b: Study of the geometry effect on
613 land surface temperature retrieval in urban environment. *ISPRS J. Photogramm.*
614 *Remote Sens.*, **109**, 77–87, doi:10.1016/j.isprsjprs.2015.09.001.
615 Wan, Z., D. Ng, and J. Dozier, 1994: Spectral emissivity measurements of land-surface
616 materials and related radiative transfer simulations. *Adv. Sp. Res.*, **14**, 91–94,
617 doi:10.1016/0273-1177(94)90197-X.
618

List of Figures

Fig. 1 The flowchart of the procedure for the LSE estimation method. Classes 1–11, 13, 14 and 16–18 are the land cover areas applied the NDVI thresholds method. Class 12 is the paddy field that have specific seasonal variation, such as the flooding and rice transplanting period, the growing period and the fallow period. Classes 15 and 19 are wetland and snow/ice, respectively. The LSE in these two classes are considered as unchanged value by the seasonal change of vegetation.

Fig. 2 A schematic view of direct radiances and first reflections in a Lambertian box for describing a rough surface.

Fig. 3 The SZA and FVC dependence of the cavity effect (dε) for each land cover. The left figures show the SZA dependence for band 13, 14 and 15. The right figures show the FVC dependence for band 13, 14 and 15.

Fig. 4 The upper graph is the time changes of LSEs for band 13, 14 and 15 over a cropland in Japan (42.74°N, 143.14°E) from August to December, 2015. The lower graph is the time changes of NDVI and NDSII corresponding to the above graph.

638

639 Fig. 5 The upper graph is the time changes of LSEs for band 13, 14 and 15 over a paddy
640 field in Japan (37.58°N, 138.85°E) from April to June, 2016. The lower graph is the time
641 changes of NDVI and NDWI corresponding to the above graph.

642

643 Fig. 6 The LSE error for each GLCNMO class and TIR band. The left figures show the
644 LSE error in green state and the right figures show the LSE error in senescent state.

645

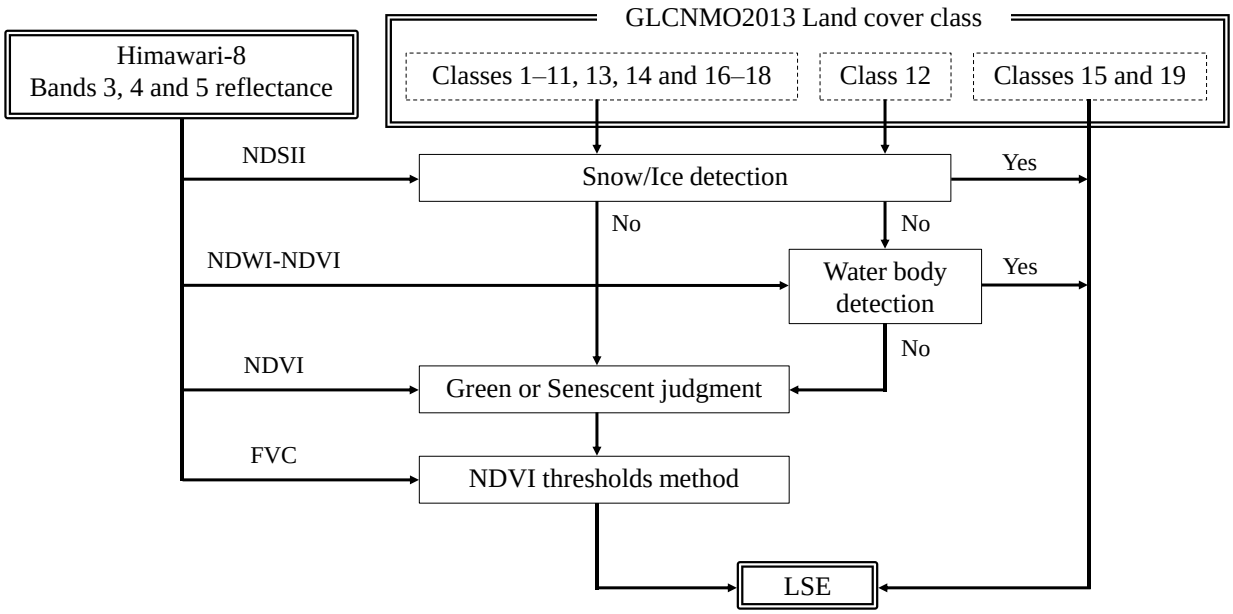

Fig. 1 The flowchart of the procedure for the LSE estimation method. Classes 1–11, 13, 14 and 16–18 are the land cover areas applied the NDVI thresholds method. Class 12 is the paddy field that have specific seasonal variation, such as the flooding and rice transplanting period, the growing period and the fallow period. Classes 15 and 19 are wetland and snow/ice, respectively. The LSE in these two classes are considered as unchanged value by the seasonal change of vegetation.

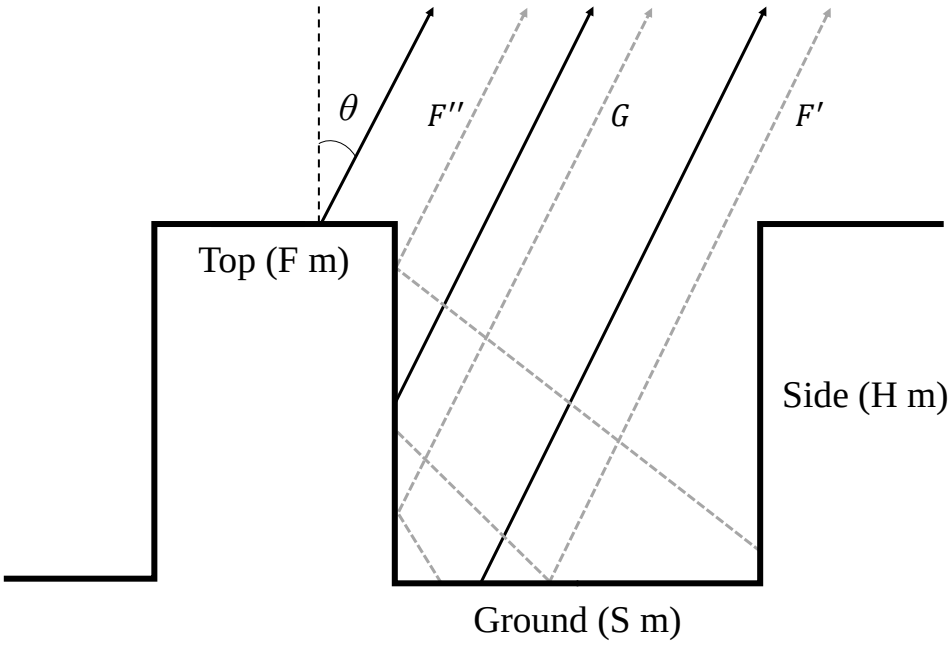

654

655 Fig. 2 A schematic view of direct radiances and first reflections in a Lambertian box for

656 describing a rough surface.

657

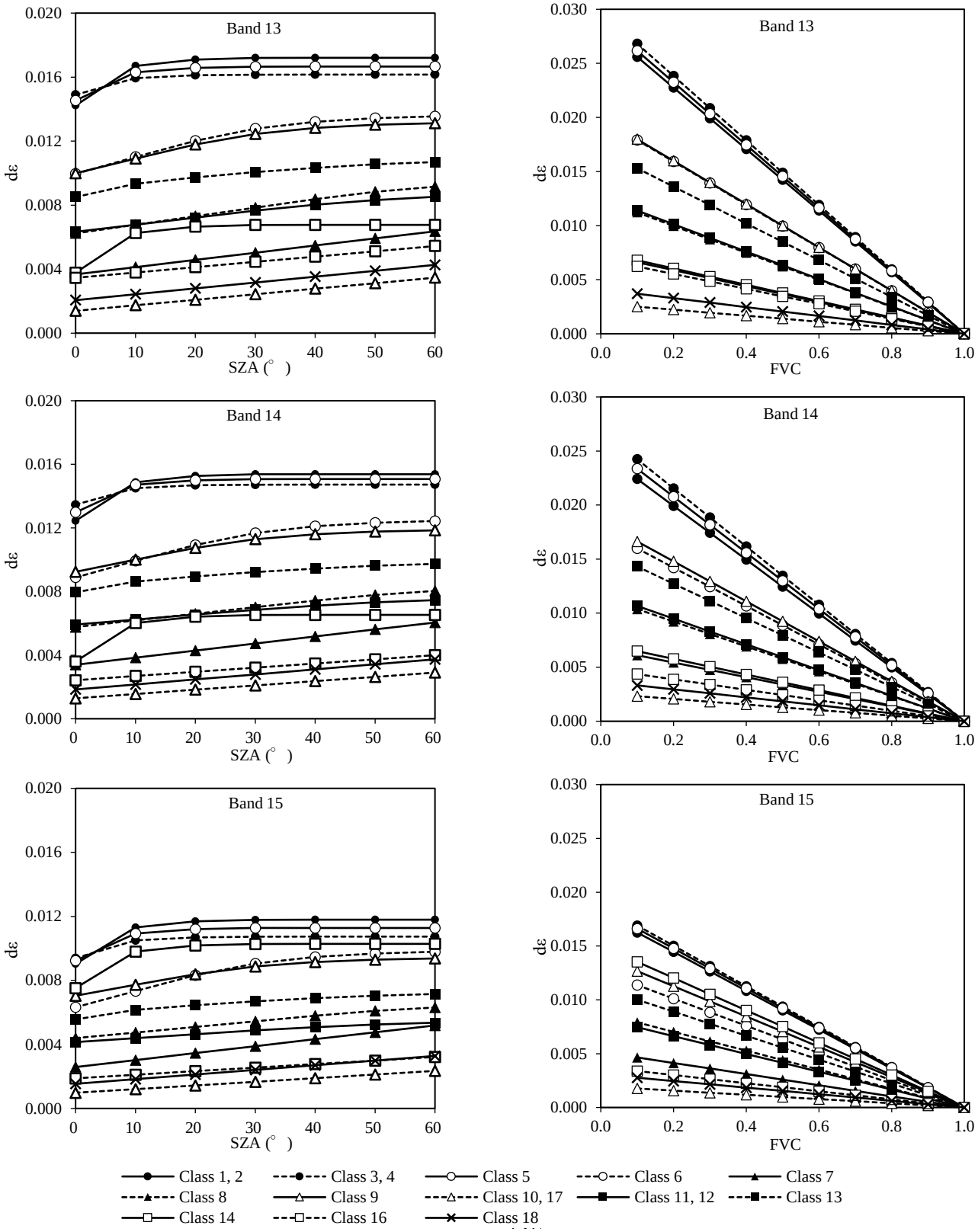

658 Fig. 3 The SZA and FVC dependence of the cavity effect (dε) for each land cover. The left

659 figures show the SZA dependence for band 13, 14 and 15. The right figures show the

660 FVC dependence for band 13, 14 and 15.

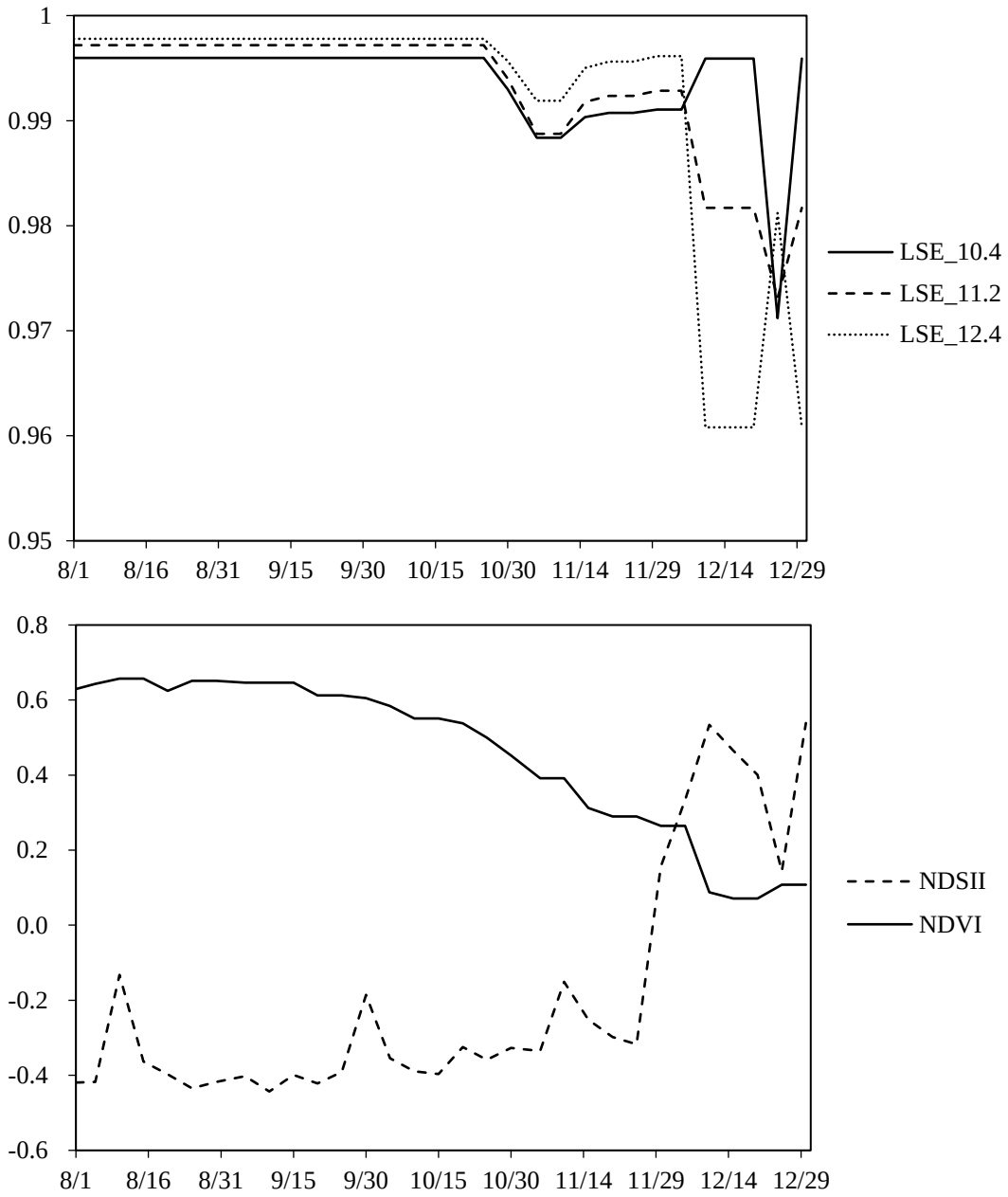

661

662 Fig. 4 The upper graph is the time changes of LSEs for band 13, 14 and 15 over a

663 cropland in Japan (42.74°N, 143.14°E) from August to December, 2015. The lower graph is

664 the time changes of NDVI and NDSII corresponding to the above graph.

665

666

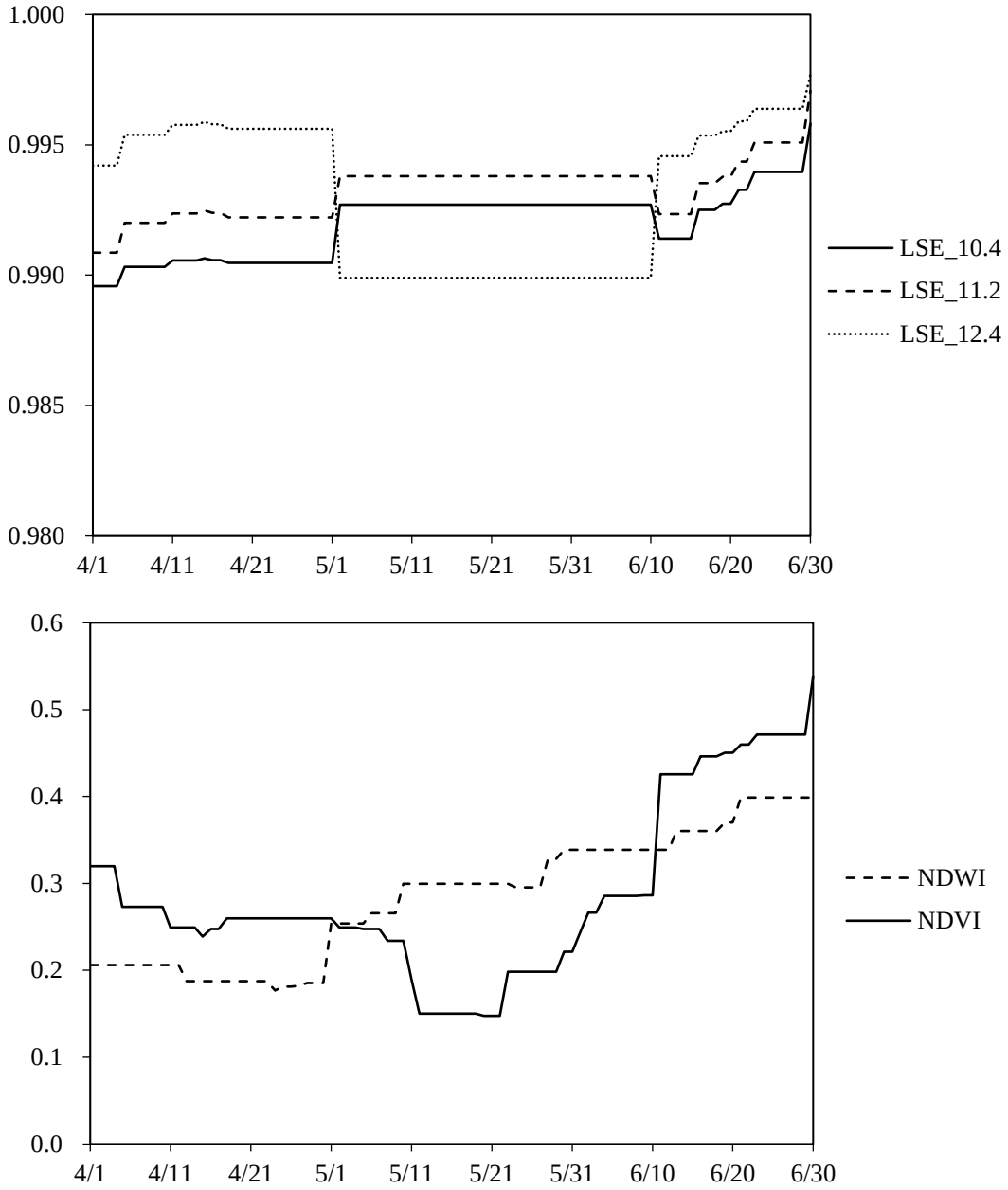

667

668 Fig. 5 The upper graph is the time changes of LSEs for band 13, 14 and 15 over a paddy

669 field in Japan (37.58°N, 138.85°E) from April to June, 2016. The lower graph is the time

670 changes of NDVI and NDWI corresponding to the above graph.

671

672

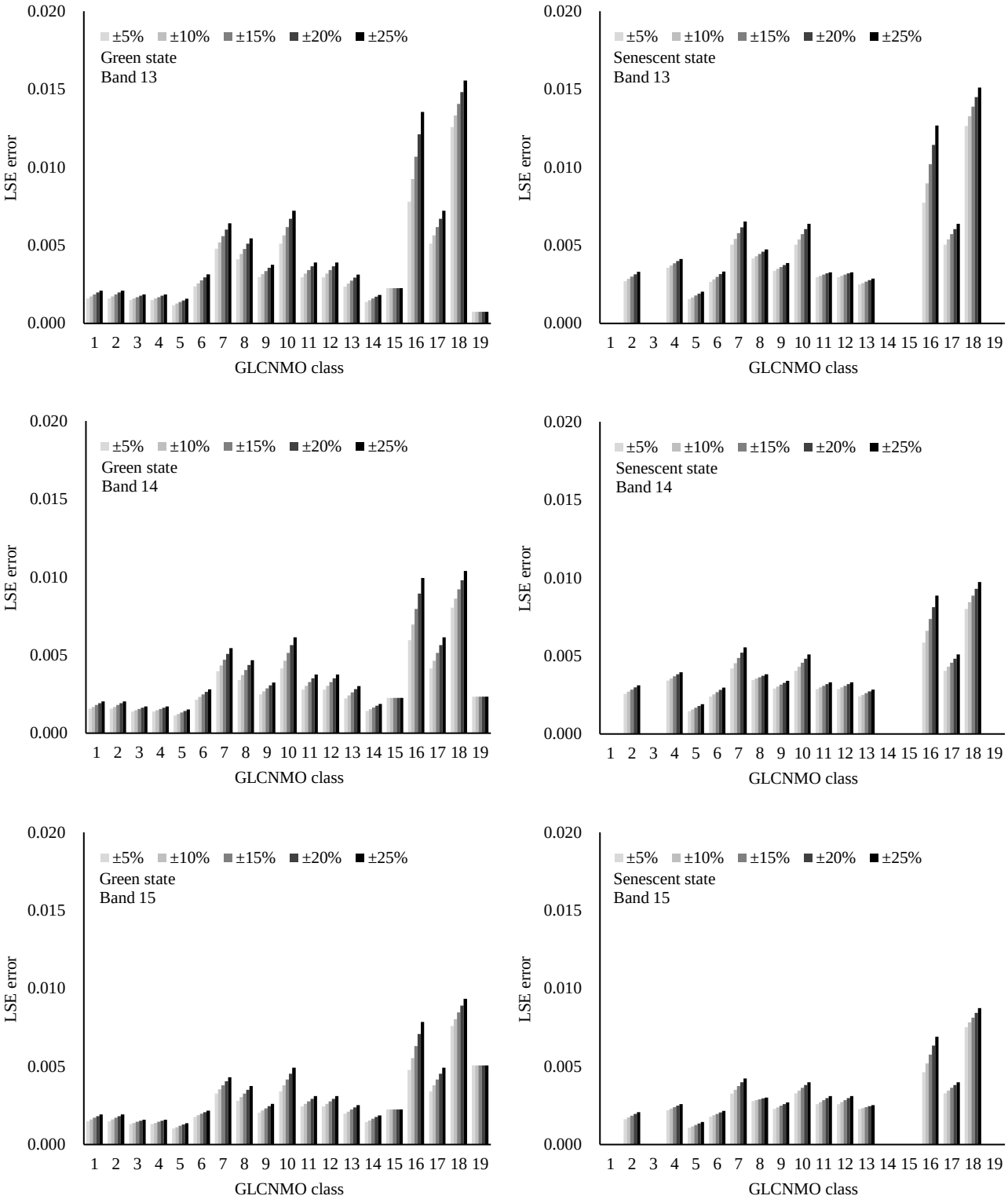

673 Fig. 6 The LSE error for each GLCNMO class and TIR band. The left figures show the

674 LSE error in green state and the right figures show the LSE error in senescent state.

675

676

677 List of Tables

678

696

697 Table 9 The cavity effect ($d\varepsilon_u$) in urban area for three TIR bands.

698

699 Table 10 The differences of ε_u and $d\varepsilon_u$ between two types of urban structures.

700

701

702

703

704

705

706

707

708

709

710

711

712

713

714

715

716 Table 1 Percentage of each land cover class in Himawari-8 main observation area (85 E–

717 155 W, 60 S–60 N). The water body (class 20) is excluded.

718

GLCNMO class	Percentage (%)
1. Broadleaf Evergreen Forest	12.65
2. Broadleaf Deciduous Forest	8.86
3. Needleleaf Evergreen Forest	3.17
4. Needleleaf Deciduous Forest	4.60
5. Mixed Forest	4.75
6. Tree Open	8.32
7. Shrub	9.53
8. Herbaceous	11.41
9. Herbaceous with Sparse Tree/Shrub	0.66
10. Sparse Vegetation	8.14
11. Cropland	10.61
12. Paddy Field	3.95
13. Cropland/Other Vegetation Mosaic	6.18
14. Mangrove	0.15
15. Wetland	0.56
16. Bare area, Consolidated (gravel, rock)	4.39
17. Bare area, Unconsolidated (sand)	1.50
18. Urban	0.44
19. Snow/Ice	0.13
Total land surface coverage	100.00

719

720 Table 2 The materials for vegetation of each land cover.

721

GLCNMO class	**Green**	**Senescent**
1. Broadleaf Evergreen Forest	Oak, Bronze Loquat, Evergreen Pear	—
2. Broadleaf Deciduous Forest	Oak, Bronze Loquat, Evergreen Pear	Oak, Maple, Bark
3. Needleleaf Evergreen Forest	Pine (New), Cypress	—
4. Needleleaf Deciduous Forest	Pine (New), Cypress	Pine (Old), Bark
5. Mixed Forest	The mean of classes 1 and 3	The mean of classes 1, 2, 3 and 4
6. Tree Open	The mean of classes 1 and 3	The mean of classes 1, 2, 3 and 4
7. Shrub	The mean of classes 1 and 3	The mean of classes 1, 2, 3 and 4
8. Herbaceous	20 % of classes 1 and 3 + 80 % of Green grass	20 % of classes 2 and 4 + 80 % of Dry grass
9. Herbaceous with Sparse Tree/Shrub	40 % of classes 1 and 3 + 60 % of Green grass	40 % of classes 2 and 4 + 60 % of Dry grass
10. Sparse vegetation	20 % of classes 1 and 3 + 80 % of Green grass	20 % of classes 2 and 4 + 80 % of Dry grass
11. Cropland	Green grass	Dry grass
12. Paddy field	Flooding and rice transplanting: class 15, Growing: Green grass	Flooding and rice transplanting: class 15, Growing or fallow: Dry grass
13. Cropland/Other Vegetation Mosaic	33 % of class 5 + 66 % of Green grass	33 % of class 5 + 66 % of Dry grass
14. Mangrove	Oak, Bronze Loquat, Evergreen Pear	—
16. Bare area (gravel, rock)	20 % of classes 1 and 3 + 80 % of Green grass	20 % of classes 2 and 4 + 80 % of Dry grass
17. Bare area (sand)	20 % of classes 1 and 3 + 80 % of Green grass	20 % of classes 2 and 4 + 80 % of Dry grass
18. Urban	50 % of class 5 + 50 % of Green grass	50 % of class 5 + 50 % of Dry grass

722

723 Table 3 The materials for ground of each land cover.

724

GLCNMO class	**Materials**
Classes 1 and 2	Inceptisols, Entisols and Mollisols
Classes 3 and 4	Inceptisols
Classes 5 and 6	The mean of classes 1, 2, 3 and 4
Classes 7, 8, 9, 10 and 17	Aridisols
Classes 11 and 13	Mollisols
Class 12	Flooding and rice transplanting: class 15, Growing or fallow: Mollisols
Class 14	Water
Class 15	Water and Green grass
Class 16	Aridisols, Igneous and Sedimentary
Class 18	Construction concretes, Road asphalts and Tar
Class 19	Snow and Ice

725

726 Table 4 Values of separation between two adjacent boxes S, height of the boxes H and

727 width of the box F.

728

Class	S (m)	H (m)	F (m)
Classes 1, 2, 3, 4, 5 and 14	0.5–1.5	2.5–10	1–4
Classes 6 and 9	3–7	2.5–10	1–4
Class 7	3–7	0.5–2.0	0.5–2.0
Class 8	8–16	2.5–10	1–4
Classes 10, 16, 17 and 18	9–21	0.5–2.0	0.5–2.0
Classes 11 and 12	1–3	0.5–2.0	0.5–2.0
Class 13	The mean of 5 and 11		

729

730 Table 5 The materials and building shapes of each face of urban structure.

731

	Top	Side	Ground
Materials	Roofing materials	Construction concretes	Road asphalts and Tar
Building shapes	F = 10—20 m	H = 7—15 m	S = 10—20 m

732

733 Table 6 The vegetation emissivity and deviation for each land cover.

734

GLCNMO class	Band 13				Band 14				Band 15			
	Green		Senescent		Green		Senescent		Green		Senescent	
	ε_v	Dev.	ε_v	Dev.	ε_v	Dev.	ε_v	Dev.	ε_v	Dev.	ε_v	Dev.
1, 14	0.9893	0.0018	—	—	0.9895	0.0020	—	—	0.9901	0.0020	—	—
2	0.9893	0.0018	0.9870	0.0045	0.9895	0.0020	0.9878	0.0045	0.9901	0.0020	0.9897	0.0023
3	0.9955	0.0019	—	—	0.9955	0.0018	—	—	0.9952	0.0021	—	—
4	0.9955	0.0019	0.9875	0.0067	0.9955	0.0018	0.9882	0.0066	0.9952	0.0021	0.9912	0.0041
5, 6, 7	0.9924	0.0012	0.9898	0.0020	0.9925	0.0013	0.9903	0.0020	0.9927	0.0013	0.9916	0.0013
8, 10, 16, 17	0.9937	0.0010	0.9784	0.0012	0.9951	0.0010	0.9763	0.0012	0.9959	0.0010	0.9802	0.0010
9	0.9934	0.0009	0.9806	0.0017	0.9945	0.0009	0.9792	0.0016	0.9951	0.0009	0.9828	0.0011
11, 12	0.9940	0.0015	0.9762	0.0015	0.9958	0.0015	0.9733	0.0015	0.9967	0.0015	0.9776	0.0015
13	0.9935	0.0009	0.9807	0.0010	0.9947	0.0009	0.9790	0.0010	0.9953	0.0009	0.9823	0.0009
18	0.9932	0.0008	0.9830	0.0012	0.9942	0.0009	0.9818	0.0011	0.9947	0.0009	0.9846	0.0009

735

736 Table 7 The ground emissivity and deviation for each land cover.

737

GLCNMO class	Band 13		Band 14		Band 15	
	ε_g	Dev.	ε_g	Dev.	ε_g	Dev.
1, 2	0.9680	0.0075	0.9720	0.0060	0.9797	0.0058
3, 4	0.9667	0.0079	0.9699	0.0070	0.9790	0.0051
5, 6	0.9674	0.0053	0.9709	0.0045	0.9793	0.0038
7, 8, 9, 10, 17	0.9673	0.0088	0.9698	0.0068	0.9770	0.0056
11, 12, 13	0.9712	0.0053	0.9731	0.0049	0.9812	0.0046
16	0.9187	0.0120	0.9432	0.0093	0.9559	0.0074
14	0.9915	0.0050	0.9919	0.0050	0.9831	0.0050
15	0.9927	0.0023	0.9938	0.0023	0.9899	0.0023
19	0.9959	0.0007	0.9817	0.0023	0.9608	0.0051

738

739 Table 8 The emissivity and deviation for each face in urban area.

740

	Band 13		Band 14		Band 15	
	ε	Dev.	ε	Dev.	ε	Dev.
Top	0.9336	0.0386	0.9499	0.0224	0.9635	0.0205
Side	0.9485	0.0096	0.9582	0.0046	0.9660	0.0053
Ground	0.9548	0.0154	0.9552	0.0133	0.9619	0.0182

741

742 Table 9 The cavity effect ($d\varepsilon_u$) in urban area for three TIR bands.

743

Band	SZA (°)						
	0	10	20	30	40	50	60
13	0.0104	0.0115	0.0125	0.0136	0.0147	0.0155	0.0161
14	0.0104	0.0109	0.0114	0.0119	0.0124	0.0128	0.0131
15	0.0089	0.0092	0.0096	0.0099	0.0102	0.0106	0.0108

744

745 Table 10 The differences of ε_u and $d\varepsilon_u$ between two types of urban structures.

746

Geometrical shape (m)		Band 13				Band 14				Band 15			
		SZA=0°	20°	40°	60°	0°	20°	40°	60°	0°	20°	40°	60°
Type A	ε_u	0.9616	0.9630	0.9644	0.9653	0.9667	0.9691	0.9716	0.9798	0.9758	0.9773	0.9788	0.9798
F: 10, H: 15, S: 20	$d\varepsilon_u$	0.0147	0.0174	0.0200	0.0218	0.0153	0.0162	0.0171	0.0146	0.0112	0.0125	0.0138	0.0146
Type B	ε_u	0.9473	0.9480	0.9488	0.9493	0.9580	0.9592	0.9605	0.9715	0.9694	0.9702	0.9710	0.9715
F: 20, H: 7, S: 10	$d\varepsilon_u$	0.0070	0.0084	0.0097	0.0107	0.0073	0.0078	0.0084	0.0072	0.0054	0.0060	0.0067	0.0072
Type A - Type B	ε_u	0.0143	0.015	0.0156	0.016	0.0087	0.0099	0.0111	0.0083	0.0064	0.0071	0.0078	0.0083
	$d\varepsilon_u$	0.0077	0.009	0.0103	0.0111	0.008	0.0084	0.0087	0.0074	0.0058	0.0065	0.0071	0.0074

747

748